Laser Photoablation of Guidance Microchannels into Hydrogels Directs Cell Growth in Three Dimensions

Offra Sarig-Nadir,[†] Noga Livnat,[‡] Ruthy Zajdman,[†] Shy Shoham,[†] and Dror Seliktar[†*]
[†]Faculty of Biomedical Engineering, and [‡]Norman Seiden Multidisciplinary Program in Nanoscience and Nanotechnology, Technion-Israel Institute of Technology, Haifa, Israel

ABSTRACT Recent years have seen rapid progress in the engineering and application of biomaterials with controlled biological, physical, and chemical properties, and the development of associated methods for micropatterning of three-dimensional tissue-engineering scaffolds. A remaining challenge is the development of robust, flexible methods that can be used to create physical guidance structures in cell-seeded scaffolds independently of environmental constraints. Here we demonstrate that focal photoablation caused by pulsed lasers can generate guidance structures in transparent hydrogels, with feature control down to the micron scale. These photopatterned microchannels guide the directional growth of neurites from dorsal root ganglia. We characterize the effect of laser properties and biomaterial properties on microchannel formation in PEGylated fibrinogen hydrogels, and the effect of photoablation on neural outgrowth. This strategy could lead to the development of a new generation of guidance channels for treating nerve injuries, and the engineering of structured three-dimensional neuronal or nonneuronal networks.

INTRODUCTION

Surface patterning of polymeric biomaterials has been exploited successfully to study cellular responses to local physical stimuli (1,2) and guide cellular behavior on biomimetic implants (3). A variety of patterning techniques have been developed to create polymeric interfaces with prescribed surface features to guide cellular migration and morphogenesis (4). However, the spatial sensitivity of morphogenic cells extends beyond two-dimensional (2D) patterned surfaces and encompasses complex geometrical landscapes in the three-dimensional (3D) extracellular matrix (ECM) of many hard and soft tissues (5). The need to broaden the field of biomaterial patterning into the third dimension has prompted efforts to adapt 2D patterning techniques to create geometrical features within a biomaterial with spatial resolution on the order of single-cell dimensions (6).

The importance of 3D micropatterning of biomaterials in tissue regeneration is exemplified in the design of nerve guidance conduits (NGCs) for peripheral nerve repair. Biomaterial-based conduits used to treat resections of peripheral nerve tissue are designed to promote directional sprouting of axons with the use of inscribed morphogenic cues that guide neuronal regeneration (7–9). Despite extensive research with preclinical results, the current state-of-the-art NGCs still cannot deliver nerve regeneration performance comparable to that of the gold standard, nerve autograft. Toward that objective, we have developed a biosynthetic hydrogel biomaterial that shows promise as an NGC biomaterial for peripheral nerve repair. The biosynthetic material is composed of both natural and synthetic constituents, and is designed to control neuronal and nonneuronal invasion based on simple compositional modifications. In recent work we demonstrated that biosynthetic fibrinogen hydrogels (i.e., fibrinogen conjugated to poly(ethylene glycol) (PEG)) support extensive outgrowth of both sprouting neurites and invading glial cells in a 3D dorsal root ganglion (DRG) outgrowth assay, and that the hydrogel composition precisely controls the outgrowth of the DRG cells (10). This PEGylated fibrinogen hydrogel still requires subcellular geometric features capable of controlling the direction of the neural outgrowth in 3D.

Existing microfabrication strategies for defining directional guidance into 3D hydrogel matrices can be grouped into two categories. The first group includes layered fabrication methods such as 3D laser printing (11,12), electrochemical deposition (13), photolithography, and soft-lithographic patterning (14–16) of 3D microfluidic scaffolds. The second category includes optical methods capable of bulk-patterning cell-seeded scaffolds that have been preformed with the desired final dimensions (17–20). Bulk patterns using optical methods, which in principle can be applied in situ, have significant advantages in terms of dealing effectively with complex cellular distributions, gel swelling, and fine resolution (when using multiphoton absorption (20)), but are currently limited to photopatterning of biochemical cues (21), 2D laser drilling into polymer structures (22), and 3D microfabrication of cellularized materials using a layered approach (23).

Here we introduce a simple yet powerful optical approach for generating geometrically complex physical guidance channels in situ, anywhere within a cellularized hydrogel material, based on laser photoablation. This technique allows for feature control down to the micron scale in essentially any semitransparent hydrogel material. We study the effect of laser properties and biomaterial properties on microchannel formation and in PEGylated fibrinogen hydrogels using

Submitted October 16, 2008, and accepted for publication March 11, 2009.

*Correspondence: dror@bm.technion.ac.il

Offra Sarig-Nadir and Noga Livnat contributed equally to this work.

Editor: Elliot L. Elson.

0006-3495/09/06/4743/10 $2.00

doi: 10.1016/j.bpj.2009.03.019

histological, microfluidic, and protein analysis methods. We also demonstrate that the photopatterned microchannels guide the growth of neurite extensions from the DRGs, as well as their glial support, and document the effect of material and microablation parameters on the outgrowth. We discuss the relation between our experimental findings and the properties of optical breakdown in water, the putative physical process that drives photoablation and channel formation in our system, as well as additional possible applications for this approach.

MATERIALS AND METHODS

PEGylated fibrinogen hydrogels

PEG-diacrylate (PEG-DA) was prepared from linear PEG-OH MW=10 kDa (Fluka, Buchs, Switzerland) as described elsewhere (24). PEGylation of reduced bovine fibrinogen (MP Biomedicals, Solon, OH) was performed with the PEG-DA (10 kDa) at a molar ratio of 4:1 PEG-DA to fibrinogen cysteines (10). The PEGylated fibrinogen product was purified, sterilized, and characterized according to previously published protocols (25). The PEGylated fibrinogen precursor solution was diluted with sterile PBS containing additional PEG-DA to adjust the protein concentration and PEG/fibrinogen ratio levels to achieve the following hydrogel compositions: hydrogel-A: 6 mg/mL protein, 3.3% total polymer, and a ratio of 75:1 PEG to fibrinogen; hydrogel-B: 9 mg/mL protein, 3.3% total polymer, and a ratio of 45:1 PEG to fibrinogen; and hydrogel-C: 9 mg/mL protein, 5.0% total polymer, and a ratio of 75:1 PEG to fibrinogen. The formation of a hydrogel was accomplished by photopolymerization using long-wave UV light exposure for 5 min (365 nm, 4–5 mW/cm^2) and a 0.1% (w/v) photo-initiator (Irgacure 2959; Ciba Specialty Chemicals, Basel, Switzerland). Rheological characterization of the hydrogels was performed using an AR-G2 parallel plate rheometer (TA Instruments, New Castle, DE) with a UV curing cell (time-sweep mode, angular frequency 3 rad/s and a 2% strain).

Microchannel fabrication

The nanosecond laser system (1 ns pulses, 100 Hz frequency, 355 nm) is a PALM MicroBeam system (Carl Zeiss MicroImaging, Bernried, Germany) set with a 20× objective (NA = 0.4) and constant stage speed of 97 μm/s. The femtosecond system uses a mode-locked Ti:Sapphire laser (Mai Tai XF; Spectra-Physics, Mountain View, CA), with a pulse duration of ~100 fs, situated on a microscope with a 60× water-immersion objective (NA = 1) and a wavelength of 880 nm, with a constant stage speed of 100 μm/s. The peak power (pulse energy divided by pulse duration) values were measured and the peak intensity was estimated for each system and laser power setting (Supporting Material). The peak intensity values used with the femtosecond system were 0.6×10^{12}, 1.5×10^{12}, 2.3×10^{12}, 3.2×10^{12}, 4.0×10^{12}, 4.9×10^{12}, 5.7×10^{12}, 6.5×10^{12}, 6.8×10^{12} (840 nm), 7.3×10^{12}, and 7.8×10^{12}. The peak intensity values used with the nanosecond system were 0.05×10^{10}, 0.2×10^{10}, 0.5×10^{10}, 0.6×10^{10}, 0.9×10^{10}, 1.3×10^{10}, 1.9×10^{10}, 3.2×10^{10}, and 5.0×10^{10} W/cm^2.

Microchannel characterization

Visible alterations of the transparent hydrogel caused by the microablations were measured by the difference of Gaussians (DOG) curve-fit method (Supporting Material). Characterization of the channel dimensions by microfluidics was done in a custom-made apparatus containing a square chamber and two needles fixed in place. The PEGylated fibrinogen solution was polymerized inside the chamber, creating a square block hydrogel with inlet and outlet reservoirs at the tip of the embedded needles (see Fig. 2 *a*). A larger channel was inscribed starting from each reservoir toward the other by repeated high-energy microablation (3.2×10^{10} W/cm^2 and a stage speed of 29 μm/s in the nanosecond system). A 200 or 1500 μm long single microchannel connecting the converging large channels was inscribed at the specified energy levels of the nanosecond system experimental design. Higgins waterproof black India ink (Sanford, Oak Brook, IL) was injected through one side of the needle into the inlet reservoir (~10 μL). In some cases hydrostatic pressure (~20 cm H_2O) was used to facilitate the flow of ink from the inlet to the outlet reservoir and through the microchannel. After the ink filled the microchannel, the hydrogel was sectioned and imaged by phase-contrast microscopy, and quantitative measurements of the width (top view) and height (side view) of the ink-filled microchannels were obtained from the phase-contrast micrographs. Histological analysis was used as an alternative method to quantify the microchannel dimensions. Frozen cross sections (20 μm thick) of ablated hydrogels specimens were prepared and stained with Eosin-Y (Sigma-Aldrich, St. Louis, MO) followed by imaging with a phase-contrast microscope. The microchannel cross section was digitally documented for morphology, and the channel height was measured directly from the images using ImageJ software. At least three different constructs were sectioned for each treatment level, and the mean was calculated for each construct from approximately five single sections. The average value for each treatment level was calculated using the respective mean data.

Measurements of ablation and hydrogel breakdown

The effects of ablation on the solid phase of the PEGylated fibrinogen hydrogel were assessed by using five different nanosecond laser energy levels on circular plugs of hydrogel-B inscribed with ~400 ablated microchannels. Each plug (18 μL) was then liquefied by homogenization in 282 μL of lysis buffer containing 10 mM Tris (Sigma-Aldrich) in 0.1 N NaOH (Merck, Darstadt, Germany), 158 mM NaCl (Frutarom, Haifa, Israel), 1 mM EDTA (Sigma-Aldrich), 0.1% SDS (Spectrum Quality Products, Gardena, CA), 1% Na-deoxycholate (Sigma-Aldrich), and 1% Triton® X-100 (Bio Lab Ltd., Jerusalem, Israel). Equal volumes (22.5 μL) of the samples were loaded separately in a Criterion XT precast polyacrylamide gel (Bio-RAD, Hercules, CA), followed by staining with Coomassie brilliant blue stain (Sigma-Aldrich) and imaging using a LAS-3000 Image capture unit (Fujifilm, Japan). Molecular weights were determined with the use of a molecular weight marker (sodium dodecyl sulfate polyacrylamide gel electrophoresis (SDS-PAGE) molecular weight standards, broad range; Bio-RAD).

DRG experiments

DRGs were harvested and cultured according to published protocols (10). DRG-embedded hydrogels constructs were modified with microchannels according to the experimental design and cultured for up to 3 weeks. The experimental design to characterize the quantitative DRG cell outgrowth within channels fabricated in PEGylated fibrinogen hydrogels consisted of two independent factors: 1), the hydrogel composition (Table 1); and 2), the laser energy level used to fabricate the microchannels (see Fig. 6). Three pairs of microchannels (~1 mm long) were fabricated in each construct, and each pair was connected to the DRG through a single connecting microchannel (~200 μm long) made using the 3.2×10^{10} W/cm^2 intensity in the nanosecond laser system, and 7.8×10^{12} W/cm^2 in the femtosecond laser system. The connecting microchannel was used to create a uniform starting point for quantitative outgrowth measurements. The DRG outgrowth was quantified using phase-contrast micrographs of the DRG constructs, imaged daily for 7 consecutive days. The cellular outgrowth distance was measured from the starting point of each of the six microchannels to the farthest point of cellular invasion and normalized by the channel length. The mean cellular outgrowth distance for each condition was calculated by averaging the normalized outgrowth data for all of the DRGs in the respective treatment (hydrogel composition, laser energy level, and day of the experiment). Experiments showing the ability of DRG cells to invade complex patterns inscribed within hydrogel-B (Technion University symbol) and hydrogel-C (the word ''nerve'') were also performed. The invasion into the word ''nerve'' was visualized with time-lapse video microscopy using phase-contrast enhancement

TABLE 1 Microchannel characterization by microfluidics and histological cross sections

Hydrogel properties	Nanosecond peak intensity ($\times 10^{10}$ W/cm^2)	Microfluidics channel width (μm)	Microfluidics channel height (μm)	Cross-section channel height (μm $\pm$ SD)
Hydrogel-A				
PEG/Fib = 75:1;	1.3	5.5	9.9	26 $\pm$ 17.1
[Fib] = 6 mg/mL;	1.9	5.9	11.6	34.5 $\pm$ 6.7
%Mass = 3.3;	3.2	11.2	37.4	57.1 $\pm$ 10.9
G′ = 366 $\pm$ 24 Pa	5.0	n/a	n/a	101.8 $\pm$ 14.7
Hydrogel-B				
PEG/Fib = 45:1;	1.3	5.5	n/a	15.3 $\pm$ 1.9
[Fib] = 9 mg/mL;	1.9	4.2	20.6	33.3 $\pm$ 9.5
%Mass = 3.3;	3.2	16.8	80.9	61.4 $\pm$ 15.1
G′ = 126 $\pm$ 10 Pa	5.0	n/a	n/a	101.1 $\pm$ 35.1
Hydrogel-C				
PEG/Fib = 75:1;	1.3	n/a	n/a	22.4 $\pm$ 8.3
[Fib] = 9 mg/mL;	1.9	5.1	19.7	43.1 $\pm$ 16.6
%Mass = 5.0;	3.2	10.6	47.1	62.5 $\pm$ 18.9
G′ = 731 $\pm$ 19 Pa	5.0	n/a	n/a	87.8 $\pm$ 14.5

n/a: not available.

(Movie S2). The DRG cell outgrowth was captured every 5 min for 3 days in culture using a 10× objective and a custom-built microscope system with an incubated environmental chamber and temperature controller.

Histology and immunofluorescence

Hematoxylin and Eosin-Y (H&E) staining (Sigma-Aldrich) was performed according to the manufacturer's standard protocols. Immunofluorescence labeling was performed as described elsewhere (10). Frozen sections of DRG specimens or whole constructs were labeled with primary antibodies against βIII-tubulin (G712A; Promega, Madison, WI) and s100 (S2644; Sigma-Aldrich), followed by fluorescently conjugated secondary antibodies, goat anti-mouse Cy3 (Chemicon International, Temecula, CA) and goat anti-rabbit FITC (Jackson Immunoresearch Laboratories, West Grove, PA), or goat anti-rabbit Cy2 (Jackson Immunoresearch Laboratories). A nuclear DAPI (Sigma-Aldrich) counterstain was incorporated directly into the secondary antibody solution.

Statistical analysis

Statistical analysis was performed on data sets from at least two independent experiments in each treatment. Differences were considered statistically significant for $p < 0.05$.

RESULTS AND DISCUSSION

Biomaterial selection and patterning

To comprehensively investigate microablation for creating 3D geometric patterns within an NGC, we chose the biomaterial system for this study not only because of its biocompatibility with cell cultures, but also because of its optical properties and physicochemical versatility and flexibility. Accordingly, we employed the biosynthetic hydrogel technology made of cross-linked PEGylated fibrinogen for three reasons: the material was optically transparent, it provided excellent control over the physicochemical properties (based on the ratio of PEG to fibrinogen), and it proved exceptionally compatible with nerve and glial cells. These hydrogels were created by conjugating PEG-diacrylate (PEG-DA, 10 kDa) with denatured, reduced fibrinogen chains to form a PEGylated fibrinogen solution that was then cross-linked into a hydrogel network by a light-activated free-radical polymerization reaction. Complex patterns were inscribed into precast hydrogels by photoablation using a focused laser beam that was spatially defined with micron resolution using computer-controlled, 3D movements of a mechanical microscope stage (Fig. 1 *a*). To explore the effect of the laser parameters on microablation patterns, we applied two different optical systems: a commercially available tissue microdissector that generates nanosecond UV pulses (PALM MicroBeam; Carl Zeiss MicroImaging), and a custom-built, two-photon laser microscope that generates 100 fs pulses in the near-infrared range. The full width at half-maximum values of the focal volumes were 4 μm and 0.6 μm laterally, and 34.4 μm and 3.0 μm axially in each respective system (Fig. 1 *c*). Both systems produced a microablation in the hydrogel (i.e., a discontinuous point defect in the amorphous hydrogel structure) that gradually became more apparent in phase-contrast micrographs as the laser's intensity was increased above a threshold value. Moving the stage at a constant speed while applying the laser to the hydrogel resulted in the formation of a linear, continuous defect within the hydrogel that resembled a microchannel (Fig. 1 *b*). We fit the lateral cross sections of the microchannel images with a parametric DOG model for each inscription intensity, and estimated threshold intensity values where contrasts first rose to significantly above the baseline (see Supporting Material for details). Theoretically, the threshold intensity values required to create point defects and continuous microchannels within the hydrogel were 0.5×10^{10} and 2.3×10^{12} W/cm^2 for the nanosecond and femtosecond systems, respectively (Fig. 1 *d*). Because the ablation was created at the focal point of the microscope objective, optical transparency of the hydrogel was required for 3D inscription in the material. The physical process that likely drives channel formation in this transparent, highly hydrated material is

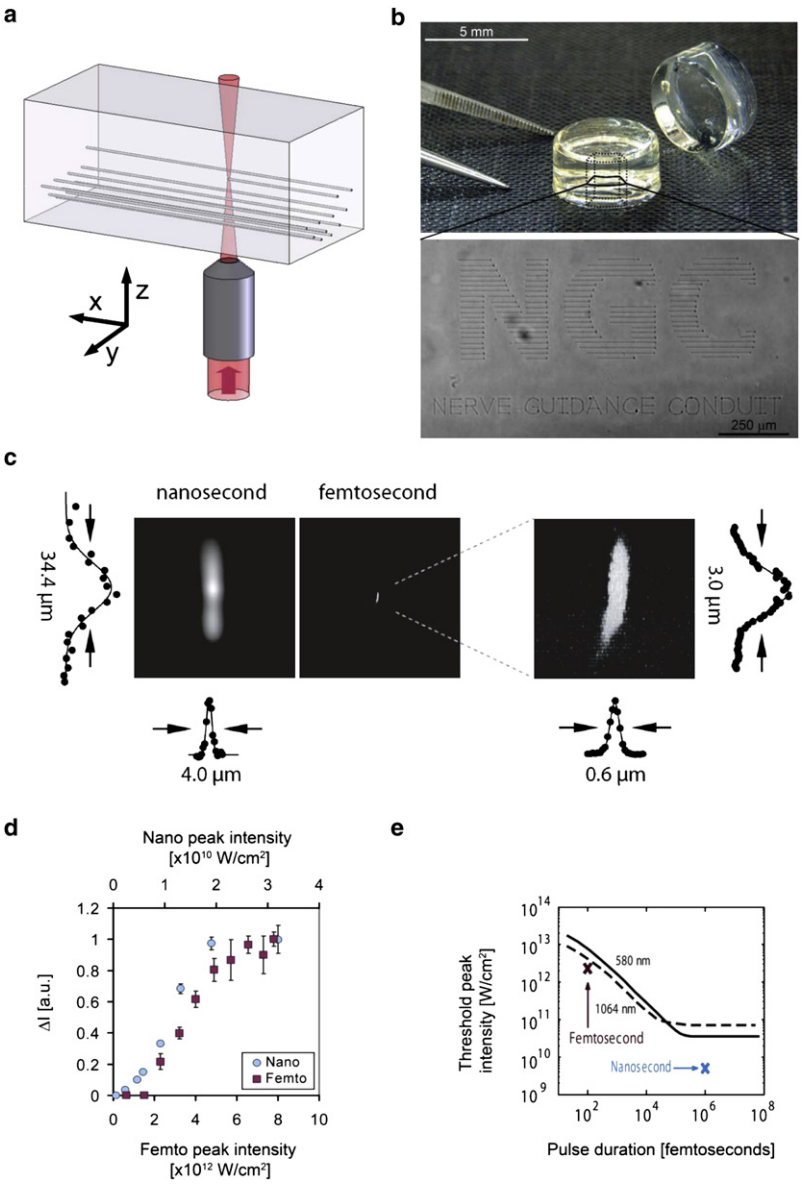

FIGURE 1 Photoablation using nanosecond and femtosecond lasers. (*a*) An illustration of 3D patterning using microscopic photoablation. (*b*) The inscription of ''NGC nerve guidance conduit'' into the middle plane of a PEGylated fibrinogen hydrogel is visible by phase-contrast microscopy. (*c*) The lateral and axial spot sizes and light intensity profiles of the nanosecond (*left*) and femtosecond (*right*) laser systems show the superior spatial resolution of the femtosecond system. (*d*) The photoablation in the hydrogels is proportional to the visible damage seen in phase-contrast micrographs when measured in terms of the maximum intensity (ΔI, arbitrary units); the graph shows ΔI as a function of laser pulse energy in the nanosecond (*blue circles*) and femtosecond (*red squares*) laser systems. (*e*) The measured (*symbols*) and theoretical (*curves*) ablation threshold values versus pulse duration for the nanosecond and femtosecond systems show that both systems behave predictably; the theoretical curves are reproduced from Fig. 3 of Noack and Vogel (27).

optical breakdown and plasma formation, which was recently described in the context of laser microsurgery and 3D micromachining (26). Our measured thresholds were in approximate agreement with theoretical predictions and experimental measurements (26–28) (see Fig. 1 *e* for a comparison with theoretical predictions). The true threshold energy level for microablation may be slightly lower than the measured values, based on the fact that some energy is absorbed in the optical path that contains both hydrogel and its underlying support (e.g., tissue culture polystyrene).

Microchannel characterization

The microchannel dimensions and morphology were characterized as a function of both the peak laser energy level and the biomaterial composition by means of a cross-section histological analysis and a microfluidics method. The histological method provided a relative measure of microchannel dimensions and morphology, albeit subject to histological variability, whereas the microfluidics method provided the undistorted dimensions (i.e., width and height) of microchannels made in the two laser systems. The channel dimensions were characterized in hydrogels using up to four peak laser intensities of the nanosecond laser: 1.3×10^{10}, 1.9×10^{10}, 3.2×10^{10}, and 5.0×10^{10} W/cm^2. Three hydrogel compositions were also used to examine the influence of material properties (i.e., cross-link density, protein composition, and total polymer concentration) on the microchannel dimensions using the four specified peak laser energy levels. The hydrogel compositions tested included hydrogel-A

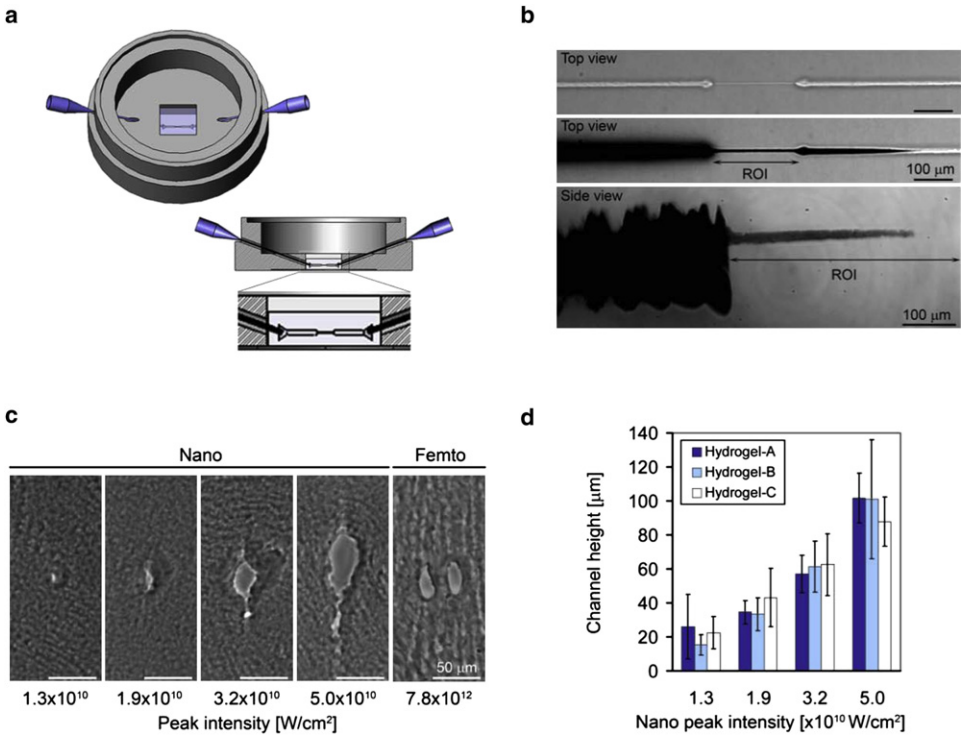

FIGURE 2 Characterizing microchannel dimensions and morphology. (*a*) A schematic illustration of the microfluidics apparatus used to characterize microchannel dimensions is shown; the cross-section illustration shows the square hydrogel sample relative to the location of the ablated microchannel in the center and middle of the gel. (*b*) The top view of a hydrogel-A sample (nanosecond laser ablation at 1.9×10^{10} W/cm^2) with a characterized channel before (*upper panel*) and after (*middle panel*) injection of black ink; the side view (*lower panel*) of a characterized microchannel after injection of ink is also shown (scale bar = 100 μm) with the highlighted region of interest (ROI) where the microchannel is created in between the larger inlet and outlet channels. (*c*) Histological cross sections of microchannels made within a hydrogel-B sample using different nanosecond (*left*) or femtosecond (*right*) laser energy levels (W/cm^2) are shown. The morphology of the microchannel is nonuniform and the height/width ratio is >1; two side-by-side microchannels made with the femtosecond system are shown (scale bar = 50 μm). (*d*) A quantitative characterization of the microchannel cross sections shows a statistically significant increase in microchannel height with increasing nanosecond laser energy levels in all hydrogel compositions tested ($p < 0.01, n \geq 3$). A comparison of the channels made in the different hydrogel compositions using the same nanosecond laser energy level reveals no significant difference in microchannel height ($p > 0.3, n \geq 3$).

(6 mg/mL protein, 3.3% total polymer, and a ratio of 75:1 PEG to fibrinogen), hydrogel-B (9 mg/mL protein, 3.3% total polymer, and a ratio of 45:1 PEG to fibrinogen), and hydrogel-C (9 mg/mL protein, 5.0% total polymer, and a ratio of 75:1 PEG to fibrinogen). A summary of the hydrogel material properties is included in Table 1. Fig. 2 *b* shows the top and side views of the microablated hydrogel before and after black ink was injected into the microchannel with the microfluidics method (shown: hydrogel-A, inscribed with 1.9×10^{10} W/cm^2 peak laser energy, nanosecond laser system). The microchannel dimensions were quantified directly from these images, and the results summarized in Table 1 reveal that both width and height increased with increasing laser energy levels in all of the hydrogel compositions. The microchannels that were fabricated using the femtosecond laser system proved to be too small at even the highest peak laser energy level (7.8×10^{12} W/cm^2) to enable microfluidic displacement of ink into the microchannel connecting the two reservoirs. However, after repeated photoablation along a single path, or a reduction in microscope stage velocity (which increased the effective laser power for ablation), the microablations were sufficiently large to enable the flow of ink into the microchannel. Thus, although both the nanosecond and femtosecond laser systems were capable of creating continuous defects in the hydrogels (Movie S1, nanosecond laser system), quantitative characterization of the dimensions of the microchannels was possible only for the nanosecond laser system when the specified laser energy levels were used.

The microchannel morphology and dimensions were further characterized by examining histological cross sections of the microablated hydrogels (Fig. 2, *c* and *d*). Morphologically, the cross sections of microchannels created by the nanosecond laser system were found to be elliptical or irregularly shaped, with an aspect ratio (i.e., the height/width ratio of the channel cross section) of >1 (Fig. 2 *c*). This aspect ratio deviated from unity as the peak laser energy level used for the ablation was increased. Quantitatively, there was a significant increase in the microchannel height with increasing peak nanosecond laser energy levels ($p < 0.01$, $n \geq 3$; Fig. 2 *d*). However, there was no significant difference between the dimensions of microchannels formed in the various hydrogel compositions tested with the nanosecond laser system ($p > 0.3$, n $\geq$ 3). With the femtosecond system, only those microchannels fabricated using a peak laser intensity of 7.8×10^{12} W/cm^2 were discernible by histological evaluation (Fig. 2 *c*); none of the other lower energies created histologically visible defects in the hydrogel.

Evidently, both laser systems produced microscopic channels in the hydrogel caused by local dissolution of the hydrogel solid phase at the focal point of the microscope objective. Furthermore, the microchannel cross-sectional dimensions should be proportional to the focal volume of the laser

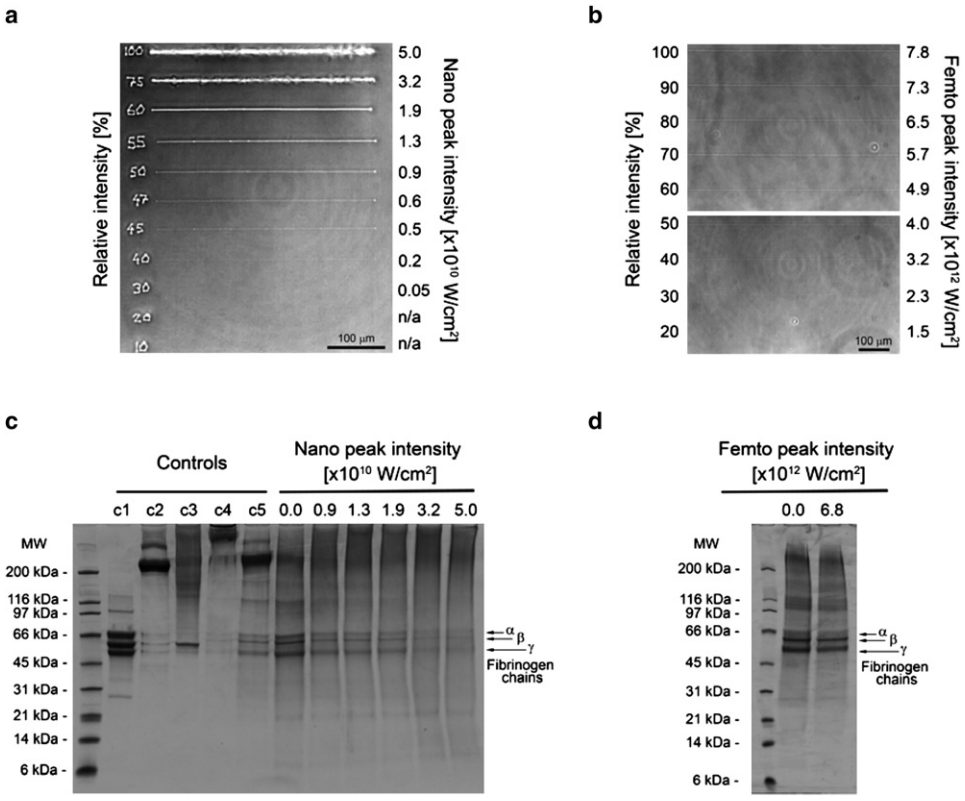

FIGURE 3 Laser ablation and optical breakdown of PEGylated fibrinogen. (*a* and *b*) The phase-contrast micrographs of microchannels inscribed into hydrogel-B samples using nanosecond (*a*) or femtosecond (*b*) laser ablation with varying power shows the visible damage to the hydrogel caused by the ablation. The percent of maximum power used is inscribed (nanosecond) or indicated (femtosecond) next to each microchannel, and shown relative to the corresponding laser's peak intensity (in W/cm^2; scale bar = 100 μm). (*c* and *d*) SDS-PAGE (4–12% gradient gel) of homogenized samples of hydrogel-B exposed to different nanosecond (*c*) or femtosecond (*d*) laser energy levels shows progressive protein breakdown at higher energy levels in the nanosecond ablation, and no significant breakdown in the 6.8×10^{12} W/cm^2 femtosecond peak energy (α, β, and γ chains of fibrinogen are indicated). Control samples shown include fibrinogen solution reduced (c1), fibrinogen solution nonreduced (c2), PEGylated fibrinogen solution reduced (c3), PEGylated fibrinogen solution nonreduced (c4), and homogenized PEGylated fibrinogen solution nonreduced (c5).

system if the disintegration of PEGylated fibrinogen in both systems is a consequence of optical breakdown. This could explain the discrepancy in microchannel dimensions created by the two systems. The effect of optical breakdown and subsequent ablation on the solid phase of the PEGylated fibrinogen hydrogel was therefore examined on ablated samples using the nanosecond laser system and various laser energies, followed by analysis using polyacrylamide gel electrophoresis in the presence of sodium dodecyl sulfate (i.e., SDS-PAGE). The densely ablated samples were processed and loaded onto SDS-PAGE gels to reveal the protein distribution (relative to unablated samples). As expected, the intensity of the protein bands representing the three natural fibrinogen chains (α, β, and γ) decreased with increasing laser energy levels used during ablation (Fig. 3 *c*). These bands, which normally appear intact in the unablated hydrogel samples (0 W/cm^2), almost completely disappeared in hydrogel samples ablated with the 3.2×10^{10} and 5.0×10^{10} W/cm^2 peak laser energy levels. A marked decrease in the intensity of the fibrinogen bands was also observed in the sample ablated with the 0.9×10^{10} W/cm^2 peak laser energy level when compared with unablated controls. This was despite the fact that no microchannels were discernible in the histological cross sections of this peak laser energy level, and that photoablation was apparent in the phase-contrast micrographs below the 0.9×10^{10} W/cm^2 peak laser energy level (Fig. 3 *a*). When the effect of optical breakdown on a hydrogel sample ablated with the femtosecond laser system (6.8×10^{12} W/cm^2, 840 nm) was examined, no observable reduction in the intensity of the α, β, and γ protein bands was apparent (Fig. 3 *d*).

Directed cell growth

To test whether discrete microchannels within a hydrogel can direct cell growth, we created microchannels in a 3D DRG hydrogel culture assay (10). A DRG specimen was situated in the hydrogel precursor solution, which was then polymerized to form the DRG-hydrogel construct. We inscribed a set of microchannels in this construct to test the ability of DRG neurons and glial cells to invade ablated defects in materials where the composition of the PEGylated fibrinogen was adjusted to ensure minimal invasion of the cells into the nonablated regions of the highly cross-linked biocompatible matrix (10). The DRG cells exhibited unidirectional migration into the microchannels in the hydrogel even when very complex geometries were inscribed juxtaposed to an embedded DRG specimen (Fig. 4, *a* and *b*, nanosecond and femtosecond laser systems). Time-lapse video microscopy was used to follow the 3-day process of cellular invasion into the latter (see Movie S2, nanosecond laser system). Specific immunolabeling with βIII-tubulin (*red*) and DAPI counterstain (*blue*) showed that both neurites and nonneuronal cells invaded the microchannels of the construct (Fig. 4 *a*, *right*). The ability to direct DRG cell outgrowth in a 3D pattern is demonstrated in Fig. 4 *c*, where

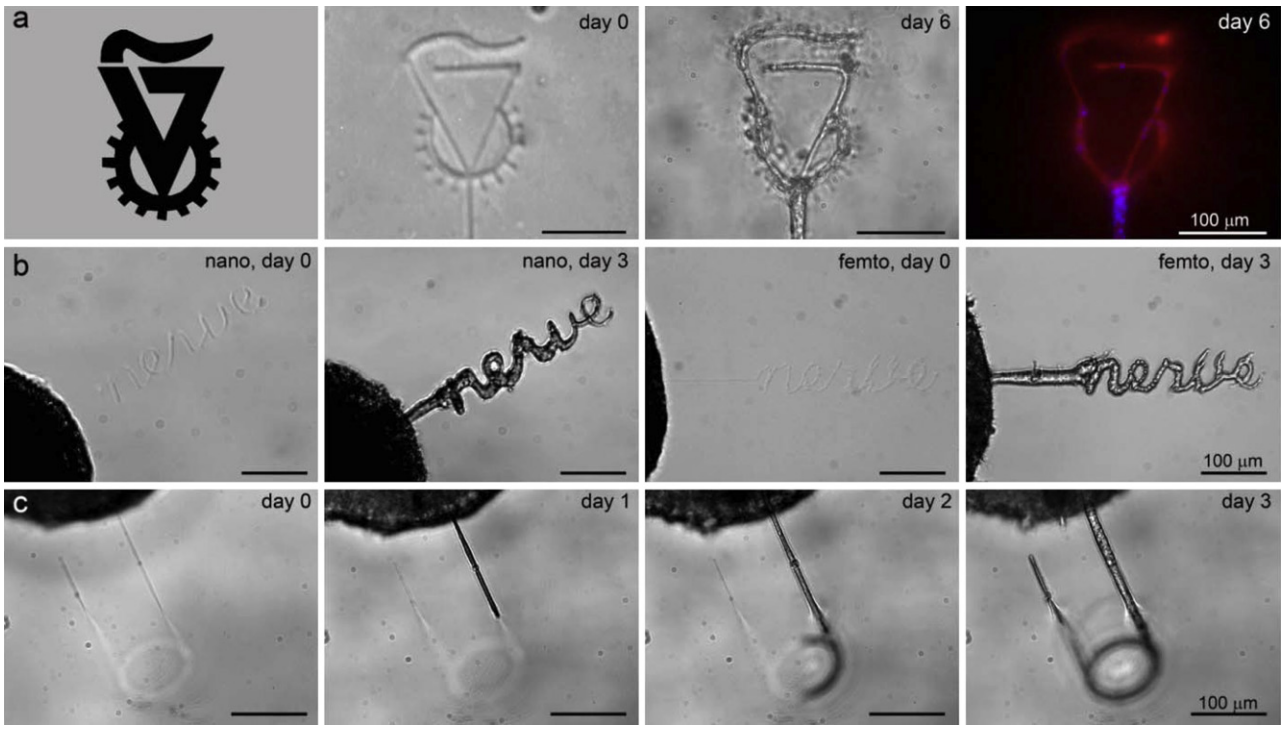

FIGURE 4 Directed DRG cell outgrowth in complex patterns of microchannels inscribed within hydrogels. (*a*) Inscription of the shape of the Technion University symbol is shown in a hydrogel-B construct before and after 6 days of DRG-cell invasion into the microchannels; immunolabeling of the DRG cells with βIII-tubulin (neural marker, *red*) and DAPI (nuclei, *blue*) is shown (scale bar = 100 μm). (*b*) An inscription of the word ''nerve'' is shown in a hydrogel-C construct using the nanosecond (*left*) and femtosecond (*right*) laser systems, with the DRG cells invading on day 3 (scale bar = 100 μm). (*c*) A 3D pattern of a microchannel is shown in a hydrogel-C construct (nanosecond laser system). DRG cell invasion into the microchannel is shown on days 1, 2, and 3, where cells traverse the focal plane as a function of the *Z*-axis position of the microchannel inside the hydrogel (scale bar = 100 μm).

DRG cells traverse the focal plane according to the *Z*-axis position of the microchannel (also shown in the time-lapse video microscopy that follows the cellular invasion throughout 3 days of experiment; see Movie S3, nanosecond laser system). Histological labeling of cross sections of the microchannels (Fig. 5, *a–d*, nanosecond laser system) with H&E or with βIII-tubulin (*red*), DAPI (*blue*), and s100 (*green*) revealed a highly contained and densely packed

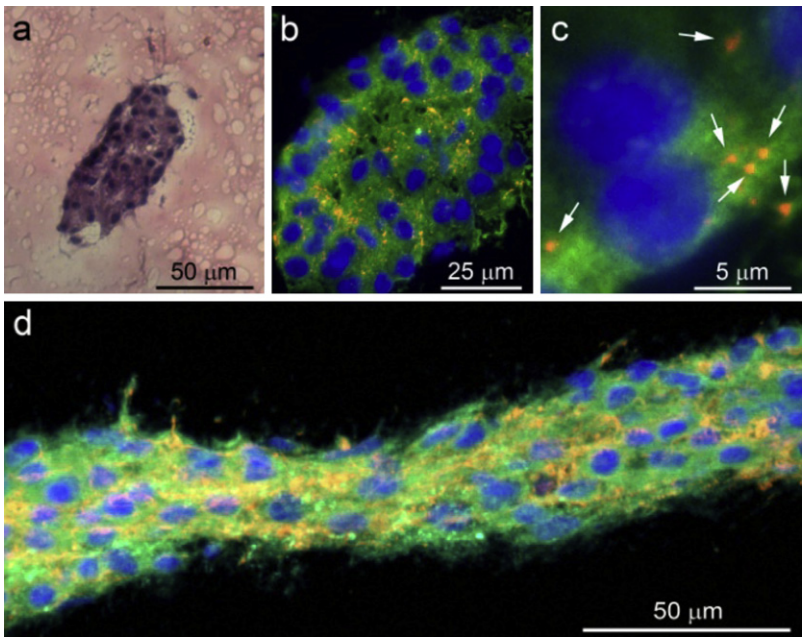

FIGURE 5 Characterization of DRG cells inside microchannels. (*a*) A histological H&E-stained cross section of the invaded microchannel (1.9×10^{10} W/cm^2 nanosecond laser energy) after 23 days in culture reveals a compacted organization of the DRG cells inside the microchannel (scale bar = 50 μm). (*b*) Immunolabeling of the cross sections reveals neurites (βIII-tubulin, *red*), glial cells (s100, *green*), and nonneuronal cells (DAPI, *blue*) invading the microchannel in an ultracompacted organization (scale bar = 25 μm). (*c*) High-magnification micrograph shows the average diameter of neurite extensions in cross section to be ~0.5 μm in diameter (scale bar = 5 μm). (*d*) Immunolabeled longitudinal cross sections of DRG cells in the microchannel after 13 days in culture show the transverse orientation of neurites (scale bar = 50 μm).

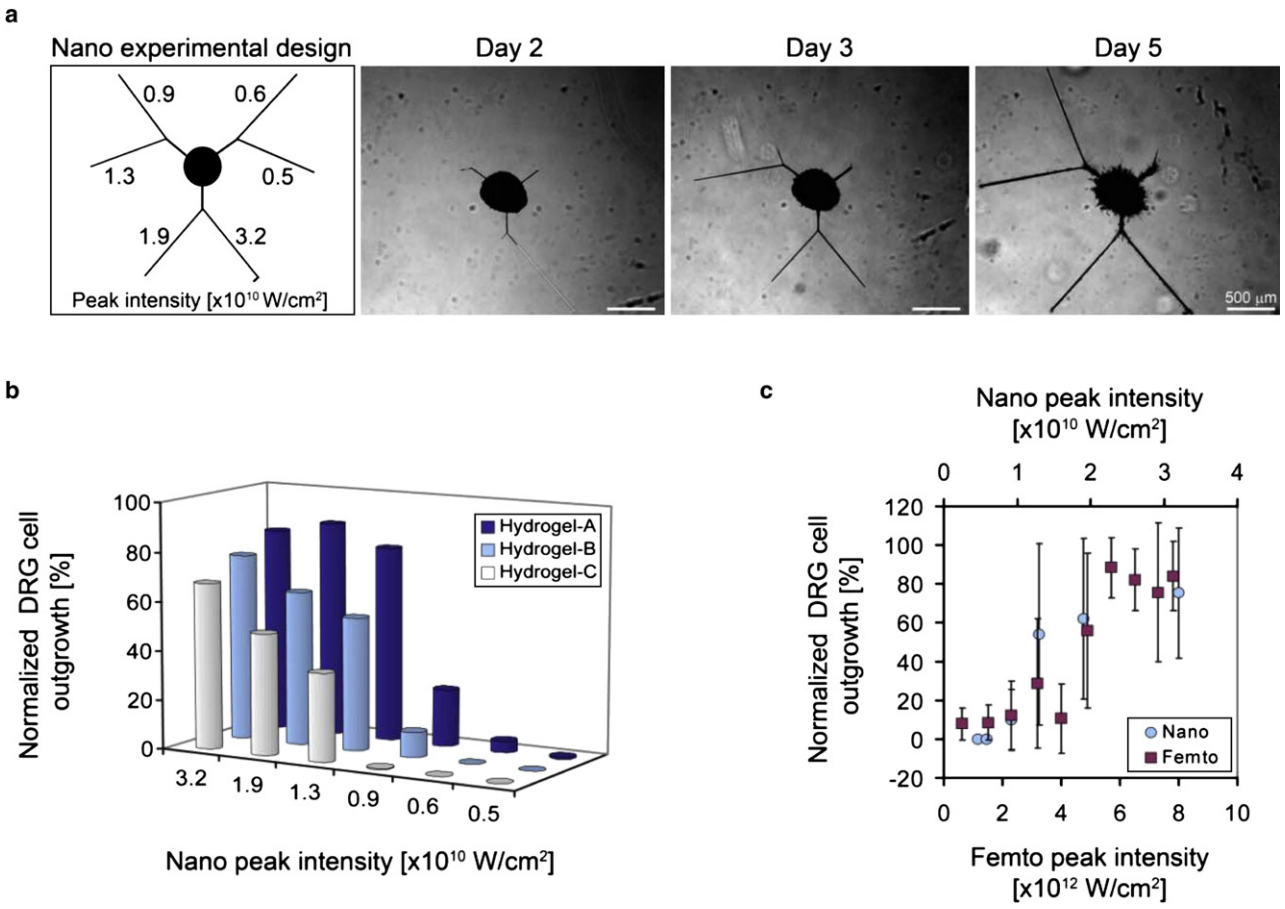

FIGURE 6 Characterization of DRG cell outgrowth as a function of the laser energy level. (*a*) Outgrowth into microchannels made with six different nanosecond laser energies (indicated in W/cm^2). Phase-contrast micrographs of DRG cells invading the microchannels in a hydrogel-A construct (nanosecond system) on days 2, 3, and 5 of the experiment reveal a transient relationship between the outgrowth and laser energy (scale bar = 500 μm). (*b*) Quantitative data representing normalized DRG cell outgrowth into the microchannels as a function of nanosecond laser energy levels on day 3 are shown for the three different hydrogel compositions tested (i.e., hydrogel-A, hydrogel-B, and hydrogel-C). The normalized outgrowth increases significantly with increased laser energy in each hydrogel composition through all days of the experiment ($p < 0.008$, $n \geq 3$). (*c*) A comparison between the nanosecond ($\times 10^{10}$ W/cm^2) and femtosecond ($\times 10^{12}$ W/cm^2) systems reveals a similar trend in both systems between the normalized DRG outgrowth and energy levels (shown: hydrogel-B, day 3).

perimeter after 23 days in culture with ~40 s100-positive glial cell nuclei present in transverse cross section (shown: hydrogel-C; 1.9×10^{10} W/cm^2 peak laser energy). Parallel cross sections of the specimen (Fig. 5 *d*) confirmed that the DRG cells occupy the entire volume of the microchannels, with the neurites (*red*) extending longitudinally. Consequently, the neurites in the transverse cross sections (Fig. 5 *c*, *red*) appear as circular spots with a diameter of ~0.5 μm and are situated in between the compacted glial cell arrangements (*green*). We further investigated the ability to regulate the invasion characteristics of both DRG neurites and glial cells based on the microchannel dimensions. Using a two-factor experimental design comprised of three different hydrogel compositions and six peak laser energy levels, we recorded the normalized DRG cell outgrowth in the microchannels over the course of a 7-day culture. Representative images of the DRG cell outgrowth into the microchannels within hydrogel-A are shown in Fig. 6 *a* for days 2, 3, and 5. Each DRG is surrounded by three sets of inscribed channels comprising the six peak energy treatment levels tested. Schematically, the nanosecond peak laser energy increases counter-clockwise around the central DRG (i.e., set 1: 0.5×10^{10} and 0.6×10^{10}; set 2: 0.9×10^{10} and 1.3×10^{10}; and set 3: 1.9×10^{10} and 3.2×10^{10} W/cm^2). Assuming that the peak laser energy is well correlated to the microchannel dimensions (Fig. 2 *d*), one can see that the DRG cell outgrowth into the microchannels was clearly influenced by the different peak energy levels, and thus also by the microchannel dimensions. However, preferential migration into the smallest microchannels by the neurites (>0.5 μm) relative to the larger glial cells (>10 μm) based on size exclusion was not observed. This is likely because the anchorage-dependent glial cells, like other anchorage-dependent mesenchymal cells, can physically and proteolytically remodel the PEGylated fibrinogen (29) and force their way into the hydrogel imperfections caused by the

microablation. This can be clearly seen in 3 days of time-lapse video showing the transient process of cellular invasion into the microchannels (Movie S2, nanosecond laser system), and is further reinforced by the enlarged cross sections of the cellularized microchannels after 23 days in culture (Fig. 5 *a*). Despite the remodeling capabilities of the DRG cells, quantitative measurements of DRG outgrowth distance support the observation that the microchannel dimensions dominate the cellular invasion response during the experimental culture times (Fig. 6 *b*). Quantitative measurements (representative data in Fig. 6 *b*, day 3 of the experiment) show that the normalized DRG outgrowth was significantly increased with increasing laser energy levels on each day of the experiment ($p < 0.008$ in the nanosecond system, $p < 0.0005$ in the femtosecond system, $n \geq 3$, data not shown). However, when we compared the outgrowth distance between microchannels fabricated in different hydrogel compositions using the nanosecond system, we noted a statistical difference only for the moderate laser energies (i.e., 0.9×10^{10}, 1.3×10^{10} and 1.9×10^{10} W/cm^2) and only on the third day of the experiment ($p < 0.05$, $n \geq 9$). For these laser energy levels, an increase in fibrinogen concentration or PEG-DA addition resulted in a decrease in the normalized DRG cell outgrowth in the microchannels. The apparent trend in DRG outgrowth response to photoablation was consistent between the femtosecond and nanosecond laser systems inasmuch as the outgrowth of processes from the DRGs was not preferential for either channel type (Fig. 6 *c*), even though the two systems were very different in terms of laser energy levels and spot sizes.

CONCLUSIONS

In summary, we have developed a versatile new strategy for generating complex 3D patterns with micron-scale resolution that can be practically applied to guide cellular outgrowth in semitransparent hydrogels. This method is based on photoablation and optical breakdown of the solid phase of a hydrogel material, which create highly localized imperfections in the amorphous hydrogel matrix. When applied on a highly cross-linked biocompatible matrix, the microablations provide a conductive niche for preferential cellular invasion based on contact guidance and differential mechanical resistance of the biologically permissive hydrogel matrix. The exact physical characteristics of the microablated regions have been difficult to fully characterize, but are known to be laser- and system-dependent, relying crucially on parameters such as pulse duration, intensity, wavelength, and numerical aperture. The physical thresholds we measured suggest that the putative physical mechanism driving the formation of channels is optical breakdown (26). This demonstration of precise 3D laser-defined neural outgrowth control may facilitate a number of applications beyond the fabrication of peripheral nerve NGCs, including tissue repair in the central nervous system and guided regeneration of other tissue and organs. Consequently, the optical transparency of the materials employed in this study makes them ideal for experimental studies involving cellular optical imaging (30) and/or optical control of neural activity (31,32). Beyond the realm of tissue regeneration, this new method can lead to the development of spatially patterned, 3D cultured neural networks (33,34) for pharmacological or computational studies that are fully observable and controllable.

SUPPORTING MATERIAL

Focal volume dimension characterization, peak light intensity values, difference of Gaussians curve fitting, and three movies are available at http://www.biophysj.org/biophysj/supplemental/S0006-3495(XX)XXXX.

Author contributions: O.S.N. was responsible for the synthesis of biomaterials, DRG isolation/culture, microchannel characterization, histological evaluation, and all experiments using the nanosecond laser system. N.L. was responsible for laser energy measurements, focal volume characterization, and all experiments using the femtosecond laser system (including design, construction, programming, and characterization). R.Z. participated in the synthesis of biomaterials and in the DRG outgrowth, immunolabeling, and microfluidics experiments with the nanosecond system. S.S. and D.S. were responsible for design, data analysis, and manuscript preparation. The authors thank Michael Krumin for assistance with the femtosecond laser system. The authors declare that they have no competing financial interests.

The authors gratefully acknowledge the financial support of the Russell Berrie Nanotechnology Institute, the Israel Science Foundation (1140/04 and 1248/06), and the Lorry I. Lokey Interdisciplinary Center for Life Science and Engineering.

REFERENCES

1. Nelson, C. M., R. P. Jean, J. L. Tan, W. F. Liu, N. J. Sniadecki, et al. 2005. Emergent patterns of growth controlled by multicellular form and mechanics. *Proc. Natl. Acad. Sci. USA*. 102:11594–11599.
2. Falconnet, D., G. Csucs, H. M. Grandin, and M. Textor. 2006. Surface engineering approaches to micropattern surfaces for cell-based assays. *Biomaterials*. 27:3044–3063.
3. Gates, B. D., Q. Xu, M. Stewart, D. Ryan, C. G. Willson, et al. 2005. New approaches to nanofabrication: molding, printing, and other techniques. *Chem. Rev*. 105:1171–1196.
4. Nie, Z., and E. Kumacheva. 2008. Patterning surfaces with functional polymers. *Nat. Mater*. 7:277–290.
5. Pedersen, J. A., and M. A. Swartz. 2005. Mechanobiology in the third dimension. *Ann. Biomed. Eng*. 33:1469–1490.
6. Khetani, S. R., and S. N. Bhatia. 2008. Microscale culture of human liver cells for drug development. *Nat. Biotechnol*. 26:120–126.
7. Bellamkonda, R. V. 2006. Peripheral nerve regeneration: an opinion on channels, scaffolds and anisotropy. *Biomaterials*. 27:3515–3518.
8. Schmidt, C. E., and J. B. Leach. 2003. Neural tissue engineering: strategies for repair and regeneration. *Annu. Rev. Biomed. Eng*. 5:293–347.
9. Yu, T. T., and M. S. Shoichet. 2005. Guided cell adhesion and outgrowth in peptide-modified channels for neural tissue engineering. *Biomaterials*. 26:1507–1514.
10. Sarig-Nadir, O., and D. Seliktar. 2008. Compositional alterations of fibrin-based materials for regulating in vitro neural outgrowth. *Tissue Eng. Part A*. 14:401–411.
11. Arcaute, K., B. K. Mann, and R. B. Wicker. 2006. Stereolithography of three-dimensional bioactive poly(ethylene glycol) constructs with encapsulated cells. *Ann. Biomed. Eng*. 34:1429–1441.

12. Mironov, V., T. Boland, T. Trusk, G. Forgacs, and R. R. Markwald. 2003. Organ printing: computer-aided jet-based 3D tissue engineering. *Trends Biotechnol*. 21:157–161.

13. Fernandes, R., L. Q. Wu, T. Chen, H. Yi, G. W. Rubloff, et al. 2003. Electrochemically induced deposition of a polysaccharide hydrogel onto a patterned surface. *Langmuir*. 19:4058–4062.

14. Kane, R. S., S. Takayama, E. Ostuni, D. E. Ingber, and G. M. Whitesides. 1999. Patterning proteins and cells using soft lithography. *Biomaterials*. 20:2363–2376.

15. Choi, N. W., M. Cabodi, B. Held, J. P. Gleghorn, L. J. Bonassar, and A. D. Stroock. 2007. Microfluidic scaffolds for tissue engineering. *Nat. Mater*. 6:908–915.

16. Suh, K. Y., J. Seong, A. Khademhosseini, P. E. Laibinis, and R. Langer. 2004. A simple soft lithographic route to fabrication of poly(ethylene glycol) microstructures for protein and cell patterning. *Biomaterials*. 25:557–563.

17. Borkenhagen, M., J. F. Clémence, H. Sigrist, and P. Aebischer. 1998. Three-dimensional extracellular matrix engineering in the nervous system. *J. Biomed. Mater. Res*. 40:392–400.

18. Luo, Y., and M. S. Shoichet. 2004. A photolabile hydrogel for guided three-dimensional cell growth and migration. *Nat. Mater*. 3:249–253.

19. Hutchison, J. B., P. F. Stark, C. J. Hawker, and K. S. Anseth. 2005. Polymerizable living free radical initiators as a platform to synthesize functional networks. *Chem. Mater*. 17:4789–4797.

20. Hahn, M. S., J. S. Miller, and J. L. West. 2006. Three-dimensional biochemical and biomechanical patterning of hydrogels for guiding cell behavior. *Adv. Mater*. 18:2679–2684.

21. Wosnick, J. H., and M. S. Shoichet. 2008. Three-dimensional chemical patterning of transparent hydrogels. *Chem. Mater*. 20:55–60.

22. Brayfield, C. A., K. G. Marra, J. P. Leonard, X. Tracy Cui, and J. C. Gerlach. 2008. Excimer laser channel creation in polyethersulfone hollow fibers for compartmentalized in vitro neuronal cell culture scaffolds. *Acta Biomater*. 4:244–255.

23. Liu Tsang, V., A. A. Chen, L. M. Cho, K. D. Jadin, R. L. Sah, et al. 2007. Fabrication of 3D hepatic tissues by additive photopatterning of cellular hydrogels. *FASEB J*. 21:790–801.

24. Almany, L., and D. Seliktar. 2005. Biosynthetic hydrogel scaffolds made from fibrinogen and polyethylene glycol for 3D cell cultures. *Biomaterials*. 26:2467–2477.

25. Dikovsky, D., H. Bianco-Peled, and D. Seliktar. 2006. The effect of structural alterations of PEG-fibrinogen hydrogel scaffolds on 3-D cellular morphology and cellular migration. *Biomaterials*. 27:1496–1506.

26. Vogel, A., J. Noack, G. Huttman, and G. Paltauf. 2005. Mechanisms of femtosecond laser nanosurgery of cells and tissues. *Appl. Phys. B*. 81:1015–1047.

27. Noack, J., and A. Vogel. 1999. Laser-induced plasma formation in water at nanosecond to femtosecond time scales: calculation of thresholds, absorption coefficients, and energy density. *IEEE J. Quantum Electron*. 35:1156–1167.

28. Kennedy, P. K., S. A. Boppart, D. X. Hammer, B. A. Rockwell, G. D. Noojin, et al. 1995. A first-order model for computation of laser-induced breakdown thresholds in ocular and aqueous media. 2. Comparison to experiment. *IEEE J. Quantum Electron*. 31:2250–2257.

29. Dikovsky, D., H. Bianco-Peled, and D. Seliktar. 2008. Defining the role of matrix compliance and proteolysis in three-dimensional cell spreading and remodeling. *Biophys. J*. 94:2914–2925.

30. Yuste, R., and A. Konnerth. 2005. Imaging in Neuroscience and Development: A Laboratory Manual. Cold Spring Harbor Laboratory Press, Cold Spring Harbor, New York.

31. Shoham, S., D. H. O'Connor, D. V. Sarkisov, and S. S. H. Wang. 2005. Rapid neurotransmitter uncaging in spatially defined patterns. *Nat. Methods*. 2:837–843.

32. Herlitze, S., and L. T. Landmesser. 2007. New optical tools for controlling neuronal activity. *Curr. Opin. Neurobiol*. 17:87–94.

33. Potter, S. M. 2001. Distributed processing in cultured neuronal networks. *Prog. Brain Res*. 130:49–62.

34. Edelman, D. B., and E. W. Keefer. 2005. A cultural renaissance: in vitro cell biology embraces three-dimensional context. *Exp. Neurol*. 192:1–6.